

# *Impact of heat storage on remote-sensing based quantification of anthropogenic heat in urban environments*

Article

Accepted Version

Yu, Z., Hu, L., Sun, T. ORCID: <https://orcid.org/0000-0002-2486-6146>, Albertson, J. and Li, Q. (2021) Impact of heat storage on remote-sensing based quantification of anthropogenic heat in urban environments. Remote Sensing of Environment, 262. 112520. ISSN 0034-4257 doi: 10.1016/j.rse.2021.112520 Available at <https://centaur.reading.ac.uk/98434/>

It is advisable to refer to the publisher's version if you intend to cite from the work. See [Guidance on citing](#).

Published version at: <http://dx.doi.org/10.1016/j.rse.2021.112520>

To link to this article DOI: <http://dx.doi.org/10.1016/j.rse.2021.112520>

Publisher: Elsevier

All outputs in CentAUR are protected by Intellectual Property Rights law, including copyright law. Copyright and IPR is retained by the creators or other copyright holders. Terms and conditions for use of this material are defined in the [End User Agreement](#).

[www.reading.ac.uk/centaur](http://www.reading.ac.uk/centaur)

**CentAUR**

Central Archive at the University of Reading

Reading's research outputs online

# Impact of Heat Storage on Remote-Sensing Based Quantification of Anthropogenic Heat in Urban Environments

Zhou Yu<sup>a</sup>, Leiqiu Hu<sup>b</sup>, Ting Sun<sup>c</sup>, John Albertson<sup>a</sup>, Qi Li<sup>a,\*</sup>

<sup>a</sup>*School of Civil and Environmental Engineering, Cornell University, Ithaca, NY, United States of America*

<sup>b</sup>*Department of Atmospheric and Earth Science, University of Alabama in Huntsville, Huntsville, AL, United States of America*

<sup>c</sup>*Department of Meteorology, University of Reading, Reading, United Kingdom*

---

## Abstract

Anthropogenic heat (AH) significantly impacts urban climates. Although combining the surface energy balance (SEB) with remote sensing data (RS-SEB) is promising for AH quantification, it has been shown to yield paradoxical low AH values in urban centers. Some speculation on the causes for the underestimation has appeared in the literature; however, none has been verified or thoroughly evaluated, largely hindering the further improvement of spatial representation of AH estimated through the RS-SEB approach. Here by casting the difference in the SEB between the observed reference state and a hypothetical scenario without AH, we developed a thermal stability analysis framework to identify the primary causes. Using AH estimations from six representative US cities based on Local Climate Zone (LCZ), we find that the reduced efficiency of the pathway from AH to sensible heat flux

---

\*ql56@cornell.edu

near high-rise buildings results in greater heat storage, which is a primary contributor to the underestimation. This study highlights the importance of heat storage in AH quantification using remote sensing data and provides evidence for potentially correcting the bias in AH with improved heat storage modeling.

*Keywords:* Anthropogenic heat flux, Surface energy balance, Heat storage

---

## 1. Introduction

More than 55% of the global population lives in urbanized areas, but account for nearly 70% of the world’s annual energy use (Quah and Roth, 2012). The energy consumed to sustain anthropogenic activities (e.g. transportation, building energy and industrial processes) and human metabolism have been well recognized as an important source term in the energy budget for an urban system across multiple spatial scales (Pigeon et al., 2007; Sailor and Lu, 2004; Allen et al., 2011), often denoted as the anthropogenic heat (AH). As an important component of the urban surface energy balance (SEB), AH impacts the urban climates non-trivially. For example, AH is an important contributor to the urban heat island effect (Bohnenstengel et al., 2014; Chow et al., 2014). The occurrence and spatial distribution of urban precipitation are also sensitive to AH (Holst et al., 2016; Feng et al., 2012; Nie et al., 2017; Zhang et al., 2018). However, accurate description of spatial and temporal evolution of AH is still challenging.

Inventory-based approaches (e.g. Iamarino et al., 2012; Quah and Roth,

2012; Sailor, 2011; Allen et al., 2011)) derived from energy-consumption data have been successfully applied to quantify AH, often offering temporal profiles of AH but lacking fine-grained spatial details due to data availability (Dong et al., 2017). The observational-based approach (e.g. (Offerle et al., 2005; Pigeon et al., 2007; Chow et al., 2014)) quantifies AH as a residual term in the SEB, which is usually adopted in the urban meteorology community, when other components of the SEB are directly available from observations such as using flux-tower measurements. However, the term representing change in heat storage in the SEB that can vary with different seasons is often neglected (e.g. Chow et al. (2014)) and only neighborhood-scale AH can be obtained using this method (i.e. integrated over flux footprint of tower sensors).

On the other hand, much finer spatial detail and wider geographical coverage have been achieved by using remote-sensing based approaches, in which different methods have been developed for mapping AH estimates for a diverse range of spatial-temporal scales (e.g. (Zhang et al., 2019; Chrysoulakis et al., 2018; Kato and Yamaguchi, 2005)). One of the widely adopted methods considers the urban SEB and uses the easily accessible remotely sensed (RS) surface temperatures from satellite platforms to quantify AH (Kato and Yamaguchi, 2005), hereafter referred as the RS-SEB method. First developed by Kato and Yamaguchi (2005), the RS-SEB method is based on the idea that AH-induced increases in air and surface temperatures predominantly raise the sensible heat flux, with only negligible effects on other terms in the SEB. In essence this is to assume that all of the AH is removed from

the control volume by the sensible heat pathway. Later applications of the RS-SEB method have unequivocally adopted this assumption (Zhou et al., 2012; Wong et al., 2015). Despite reasonable spatial distribution of AH at the regional-scale, finer grained studies have resulted in anomalously low values of AH in parts of the urban center (Kato and Yamaguchi, 2005; Wong et al., 2015; Zhou et al., 2012), contradicting both common sense and inventory-based data (Zhou et al., 2012; Dong et al., 2017). This phenomenon has been speculated to be caused by the shading of tall buildings causing deviations in skin temperature, e.g., in Kato and Yamaguchi (2005), but no clear consensus has been reached. Therefore, we explore here in greater depth the underlying key assumption of the RS-SEB for AH quantification.

If we consider a typical control volume containing the top of the roughness sublayer to the depth in the ground with zero diurnally averaged conductive heat flux, the urban SEB with the effect of anthropogenic heating is given by

$$R_n + AH = H + LE + \Delta S, \quad (1)$$

where  $R_n$ ,  $\Delta S$ ,  $H$  and  $LE$  are the net all-wave radiation, net rate of change in heat storage (hereafter as heat storage for brevity), and turbulent sensible and latent heat fluxes, respectively. In particular, depending on the way in which anthropogenic energy sources are distributed in the control volume (i.e., building energy use, traffic heat exhausts and human metabolism, etc.), AH may cause a non-negligible change in  $\Delta S$ , which is the net energy stored

61 (or released) by all substances in the control volume (e.g. the canopy air,  
 62 buildings, ground, vegetation and human beings, etc.) (Oke et al., 2017). It  
 63 can be conjectured that the transient effect of AH on  $\Delta S$  may lead to viola-  
 64 tion of the assumption of AH being directly converted to  $H$  in the RS-SEB  
 65 method. Nevertheless, few studies thus far have targeted the resolution of  
 66 this issue. Furthermore, the relative impacts of different urban land use and  
 67 land cover (LULC) types on this assumption remain relatively understudied,  
 68 which hampers our understanding of the reliability of the RS-SEB method  
 69 at the neighborhood scale within a city.

70 Motivated by the aforementioned knowledge gaps, this paper first exam-  
 71 ines the variation of AH estimates across different urban LULC types classi-  
 72 fied according to the local climate zones (LCZs) (Stewart and Oke, 2012) in  
 73 Section 2. Then, in Section 3 we present a new theoretical analysis frame-  
 74 work to examine the impact of heat storage on the RS-SEB method. Final  
 75 remarks and conclusions are presented in Section 4.

## 76 **2. AH estimation from satellite observations using the RS-SEB** 77 **method**

78 To examine the profile of AH estimates across LCZ types for a range of  
 79 cities, we first estimate AH with the classic RS-SEB method (Kato and Ya-  
 80 maguchi, 2005) for six cities in the US with contrasting sizes and background  
 81 climates (Chicago, Washington DC, Houston, Los Angeles, Philadelphia, and  
 82 Phoenix). One scene of Landsat 8 imagery under clear-sky was selected for

each city. Since perfectly cloudless condition within the selected domains for all six cities needs to be satisfied, images from satellite overpasses in fall and spring of 2017 were selected. In addition, since background climates in different cities mostly affect energy use for heating and cooling in winter and summer (Sailor, 2011), we avoid these two seasons and only focus on the ‘baseline’ anthropogenic heat in spring and fall. The components of the SEB were computed following similar procedures and methods as outlined in Kato and Yamaguchi (2005), with details of the computation presented in Appendix A.

The urban LULC types were classified according to the LCZs, which Stewart and Oke (2012) defined to be ‘regions of uniform surface cover, structure, material, and human activity that span hundreds of meters to several kilometers in horizontal scale’. The LCZ classification maps were obtained from the World Urban Database and Access Portal Tools (WUDAPT) (Ching et al., 2018), where LCZ types 1 to 10 (See Figures 1b and d) denote compact high-rise (LCZ 1), compact mid-rise (LCZ 2), compact low-rise (LCZ 3), open high-rise (LCZ 4), open mid-rise (LCZ 5), open low-rise (LCZ 6), light-weight low-rise (LCZ 7), large low-rise (LCZ 8), sparsely built (LCZ 9) and heavy industry (LCZ 10), respectively. The urban canopy parameters needed for the computation were obtained from level-zero data products provided by WUDAPT. In general, AH in a city computed from a single satellite scene is not representative of the annual average. However, in the default level-zero database of AH from the WUDAPT (here defined as  $AH_i^{default}$  for the  $i^{th}$



106 LCZ),  $AH_i^{default}$  is the annual average value of  $AH$  are adopted from the  
 107 criteria for LCZ classification (Stewart and Oke, 2012, Table 4). In fact,  $AH$   
 108 varies significantly with season, location, and level of energy consumption of  
 109 an individual city (Stewart and Oke, 2012). To remove these confounding  
 110 issues from the comparison, we focus on how  $AH^{RS-SEB}$  varies across LCZ  
 111 within any given city. To increase the statistical power of the comparison,  
 112 we compute  $AH^{RS-SEB}$  for each LCZ by averaging across all of the satel-  
 113 lite image pixels corresponding to that LCZ type in a city. Therefore, the  
 114 profile of  $AH^{RS-SEB}$  across LCZs would represent the persistent structural  
 115 differences in energy use intensity across different LCZs. Here, instead of  
 116 comparing the magnitudes of  $AH_i^{RS-SEB}$  derived from a single scene with  
 117  $AH_i^{default}$  that reflects an annual average, we focus on interrogating their  
 118 respective variations across the LCZs to reveal any similarity or contrast.

119 Before interrogating the LCZ dependence of  $AH$ , we look at the spa-  
 120 tial distribution of the estimated  $AH$  using the RS-SEB method and the  
 121 corresponding LCZ maps for Chicago and Philadelphia in Figure 1, as two  
 122 examples. We note oddly low values of  $AH$  can be clearly identified in regions  
 123 classified as compact high-rise (LCZ 1) and open high-rise (LCZ 4) in the  
 124 downtown areas. These patterns consistently occur in other selected cities  
 125 and are in stark contrast to the spatial distributions of  $AH$  estimated using  
 126 inventory-based approach (Chow et al., 2014; Pigeon et al., 2007; Roberts  
 127 et al., 2006). The RS-SEB based  $AH$  estimates for all cities were averaged by  
 128 LCZ type ( $AH_i^{RS-SEB}$ ) and are presented alongside the inventory estimates

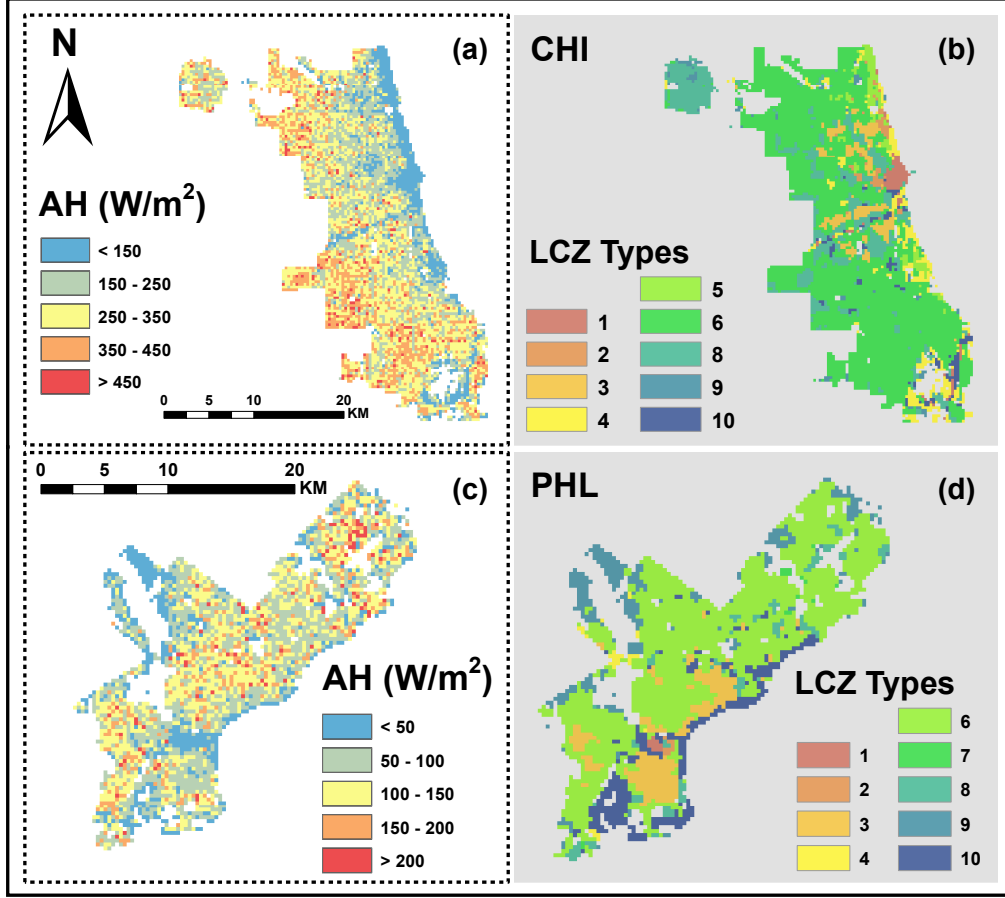


Figure 1: Two examples of the selected cities (Chicago, 20170915, 16:35 UTC and Philadelphia, 20171002, 15:40 UTC) AH results (a, c) and LCZ classifications (b, d) (1: compact high-rise; 2: compact mid-rise; 3: compact low-rise; 4: open high-rise; 5: open mid-rise; 6: open low-rise; 7: light-weight low-rise; 8: large low-rise; 9: sparsely built; 10: heavy industry)

129 of  $AH_i^{default}$  in Table 2. The magnitudes of  $AH_i^{RS-SEB}$  vary significantly  
 130 across the cities, as expected to reflect the city-specific AH characteristics.  
 131 Our interest here is in variability of AH across LCZ type for a given city,  
 132 and the extent to which the shape of such an AH-LCZ profile is consistent  
 133 across different cities. The high-rise LCZ's show lower AH values (  $AH_1^{default}$  ,

$AH_4^{default}$ ) than the low-rise LCZ's ( $AH_3^{default}$ ,  $AH_6^{default}$ ) across the range  
of cities, as apparent in the puzzling spatial pattern noted in Figure 1. It  
is common to have actual AH values up to several hundreds of  $\text{W}\cdot\text{m}^{-2}$ , es-  
pecially in central urban areas during daily peak hours (Wong et al., 2015;  
Zhou et al., 2012). We also note that magnitudes of  $AH_i^{RS-SEB}$  in some  
LCZs such as LCZ 8 (large low-rise) and LCZ 9 (sparsely built) in Table 1  
are large. This is likely related to the heat storage change ( $\Delta S$ ) being mod-  
elled as  $C_g R_n$  (See Appendix A.2), where the traditional fraction taken from  
the literature of  $C_g = 0.7$  has recently been questioned as being too large  
(e.g. (Oke et al., 2017, Fig. 6.12)). However, instead of focusing on tuning  
 $\Delta S$  in the RS-SEB method, we re-examine the underlying assumption of this  
method and thus use the same value of  $C_g$  as that in Kato and Yamaguchi  
(2005) for consistency.

Figure 2 shows the LCZ dependence of  $AH_i^{RS-SEB}$  normalized by the  
respective city averaged values at the observation time ( $AH_{mean}^{RS-SEB}$ ) (solid  
markers, left y-axis).  $AH_i^{default}$  is normalized by  $AH_{mean}^{default}$ , which is the  
default AH weighted by the area fractions of LCZs in each city and aver-  
aged across all studied cities,  $\overline{AH_i^{default}} / \overline{AH_{mean}^{default}}$  (open circles, right y-axis).  
Here, we are particularly interested in LCZ 1-6 as they represent two cate-  
gories of urban construction density: compact (LCZ 1, 2 and 3) and open  
(LCZ 4, 5 and 6), where the mean building height decreases with increas-  
ing LCZ number within each category (i.e. 1 to 3, and 4 to 6). Across the  
studied cities, the magnitudes of  $AH_i^{RS-SEB} / AH_{mean}^{RS-SEB}$  generally increase

Table 1:  $AH^{RS-SEB}$  across LCZs in different cities and  $AH^{default}$  (WUDAPT) (unit: W/m<sup>2</sup>)

ineB3	CHI	DC	HOU	LA	PHL	PHX	WUDAPT
ineB3 LCZ 1	28.82	81.01	24.64	185.53	-36.87	182.02	175
LCZ 2	111.00	132.30	102.69	/	24.83	/	37.5
LCZ 3	272.49	176.39	/	380.82	104.72	376.24	37.5
LCZ 4	131.58	/	39.26	/	2.41	211.43	25
LCZ 5	94.17	104.85	92.36	278.93	/	282.03	12.5
LCZ 6	297.47	114.69	161.17	345.50	107.52	389.06	12.5
LCZ 7	/	/	/	460.85	91.64	364.16	17.5
LCZ 8	271.18	173.45	139.11	370.48	123.45	362.19	25
LCZ 9	267.50	27.58	55.12	300.33	45.59	357.79	5
LCZ 10	220.79	/	53.57	307.07	52.20	310.41	350
ineB3							

Note: CHI – Chicago (20170915, 16:35 UTC); DC – District of Columbia (20170923, 15:46 UTC); HOU – Houston (20170406, 16:50 UTC); LA – Los Angeles (20171015, 18:28 UTC); PHL – Philadelphia (20171002, 15:40 UTC); PHX – Phoenix (20171003, 18:04 UTC).

with decreasing building height in each category, in stark contrast to the decrease of  $\overline{AH_i^{default}} / \overline{AH_{mean}^{default}}$  (solid circles). These results are consistent with previous findings that low values of AH occur in parts of the urban center (where taller buildings are likely to be found) (Wong et al., 2015; Zhou et al., 2012; Kato and Yamaguchi, 2005). These RS-SEB results run counter to the tendency for taller to imply more energy consumption per unit ground area, as seen in the inventory data. Here we further demonstrate that the RS-SEB method leads to low AH values in both dense and open urban construction density, which suggests a cause beyond the proposed shading effect of buildings (Kato and Yamaguchi, 2005). Now, in the following section, we proceed to more deeply examine our conjecture about the role played by the

168 net change in heat storage.

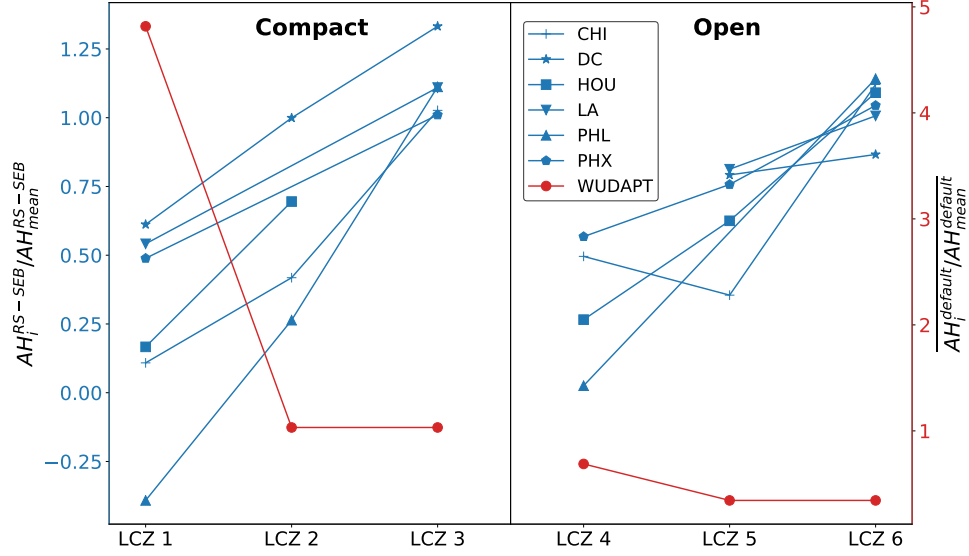


Figure 2: Variation of  $\frac{AH_i^{RS-SEB}}{AH_{mean}^{RS-SEB}}$  (Blue lines and left Y axis) and  $\frac{AH_i^{default}}{AH_{mean}^{default}}$  (red lines and right Y Axis) across different LCZs. LCZs 1-3 (LCZs 4-6) are characterized by compact (dense) urban density with descending mean building height (i.e., decreasing volume of built materials per unit area from LCZ 1 (LCZ 4) to LCZ 3 (LCZ 6)).

### 169 3. The impact of AH on heat storage in the SEB

170 To understand the reason for the systematic low values of AH in LCZs  
 171 characterized by high-rise buildings, we re-examine the underlying assump-  
 172 tion of the RS-SEB method – that AH completely causes an increase in  
 173 sensible heat flux. When integrated over time scales far exceeding one day,  
 174  $\Delta S$ , the net rate of change in heat storage becomes much smaller than other

175 terms in the SEB, and the underlying assumption becomes reasonable. How-  
 176 ever, on sub-daily time scales, especially for a snapshot in time as with remote  
 177 sensing, the partitioning of instantaneous AH into other components in the  
 178 SEB may be significant (Hanna et al., 2011; Roberts et al., 2006). Here  
 179 we consider two scenarios: the first scenario (Case No-Humans) represents  
 180 a generic urban surface without any human energy use (e.g., metabolism,  
 181 indoor energy use, transportation, industry, etc.); the second scenario (Case  
 182 With-Humans) is the same as Case No-Humans, except for the presence of  
 183 human activities (i.e., anthropogenic energy sources). Components of the  
 184 SEB in Case With-Humans thus differ from those in Case No-Humans only  
 185 due to the effects of AH. The SEB for Case With-Humans applied to the  
 186 three-dimensional control volume indicated in Figure 3a can be written as

$$R_n + R_{na} + AH = \Delta S + \Delta S_a + LE + LE_a + H + H_a, \quad (2)$$

187 and the corresponding SEB for Case No-Humans is  $R_n = \Delta S + LE + H$ ,  
 188 where the subscript ‘a’ denotes the anthropogenically-induced perturbation  
 189 to each base component. The effect of advection on the SEB is neglected.  
 190 Although the anthropogenic latent heat flux can also be significant in urban  
 191 areas especially from cooling systems in summer (Sailor, 2011; Moriwaki  
 192 et al., 2008), for the selected data in spring and fall, the direct anthropogenic  
 193 emission of water vapor is not considered. However, the potential thermally-  
 194 induced change to LE from AH is still considered via  $LE_a$ . The difference in

195 SEB between these two scenarios is

$$AH = \Delta S_a + LE_a + H_a - R_{na}. \quad (3)$$

196 The commonly adopted assumption after Kato and Yamaguchi (2005) is  
197  $AH \approx H_a$ , with  $R_{na}$ ,  $\Delta S_a$ , and  $LE_a$  assumed to be negligible. If the tur-  
198 bulent fluxes are measured, such as by using eddy-covariance measurements,  
199 then AH can be unequivocally computed from Equation 2, as the control  
200 volume contains all sources of anthropogenic heat emissions, provided  $\Delta S +$   
201  $\Delta S_a$  can be accurately determined, which is a known conundrum in urban  
202 SEB studies (Roberts et al., 2006). However, viewing from the satellite’s  
203 perspective in Figure 3a, the remotely sensed skin temperature  $T_s$  is used  
204 to model the SEB components for a two-dimensional surface projection (See  
205 Figure 3b), in which  $T_s$  encodes critical information about the partitioning of  
206 total available energy from both natural and anthropogenic sources among  
207 respective components (Wang et al., 2011; Yang and Wang, 2014). In other  
208 words, the anthropogenic heat sources in the three-dimensional control vol-  
209 ume act to alter the skin temperature  $T_s$  with modulation by the heat transfer  
210 processes (i.e. radiation, convection and conduction), which critically depend  
211 on the specific details of how the anthropogenic heat sources are distributed.

212 From the perspective of energy dissipation in the surface energy budget  
213 (Bateni and Entekhabi, 2012) for a generic surface, the total available energy  
214 is dissipated via sensible, latent, ground heat fluxes and outgoing longwave

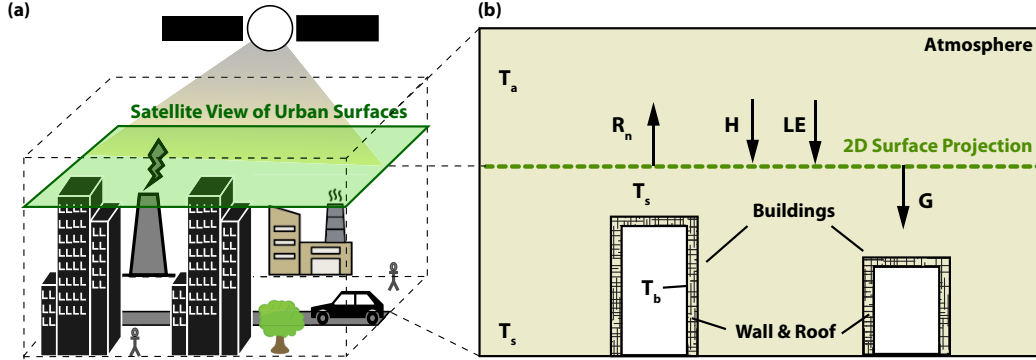


Figure 3: (a) Schematics of a three-dimensional control volume and a two-dimensional surface projection viewed from the satellite. (b) Surface energy budget in the two-dimensional projected surface, which does not explicitly contain sources of anthropogenic heat emissions. However, the three temperatures components (the skin temperature  $T_s$ , the inner building wall temperature  $T_b$  and the air temperature  $T_a$ ) are already modified by sources of anthropogenic heat emissions.  $T_s$  retrieved from the satellite represents an effective surface temperature from all surfaces including the ground and roofs.

radiation. Partitioning of total available energy depends on the relative efficiencies of dissipation via these pathways (Bateni and Entekhabi, 2012; Sun et al., 2013). Insight into the partitioning of AH can be gained by applying the force-store approach (Garratt, 1994) to the skin temperature  $T_s$  for urban surfaces (Swaid, 1995; Oke et al., 1991; Johnson et al., 1991; Miao et al., 2006) (Figure 3b), followed by a stability analysis of the SEB (Bateni and Entekhabi, 2012). The procedures are outlined briefly here and details of the derivation are presented in Appendices B and C.

First, for a generic urban surface without being influenced by anthropogenic heating (Figure 3b), the change in heat storage  $\Delta S$  (c.f. Equation 1) is equal to the conductive heat flux at the material surface (Sun et al., 2017),  $G$ , where  $G$  is constrained by the surface energy balance given by



227  $G = R_n - H - LE$ . We assume that for this material surface under consid-  
 228 eration, the net effect of human activities (i.e. anthropogenic heating) mani-  
 229 fests itself by perturbing the thermal boundary conditions of the conductive  
 230 heat transfer process. Specifically, the building interior wall temperature  $T_b$   
 231 (Johnson et al., 1991; Oke et al., 1991) and the air temperature  $T_a$  are altered,  
 232 where the deviations are denoted as  $\delta T_a$  and  $\delta T_b$ .  $T_s$  is subsequently altered  
 233 and the change is denoted as  $\delta T_s$ . The increase of air temperature by AH is  
 234 due to direct heat discharge from traffic and industry processes. Assuming  
 235 that in the selected spring and fall seasons, there is no indoor cooling by air  
 236 conditioning, the increase in the interior wall temperature is then solely due  
 237 to lighting, electrical appliances and other human activities. The perturbed  
 238 temperatures for this material surface then lead to modified surface energy  
 239 balance, thus the change in  $G$  due to anthropogenic heating can be denoted  
 240 as  $\delta G = \delta R_n - \delta H - \delta LE$ .

241 Then, the temporal evolution of the material surface temperature  $T_s$  can  
 242 be studied using the force-restore approach, which has been applied in the  
 243 urban context (Johnson et al. 1991; Oke et al. 1991), where the restoring  
 244 temperature is the interior building wall temperature  $T_b$ . The new devel-  
 245 opment here is to extend the force-restore approach to a stability analysis  
 246 framework (Bateni and Entekhabi, 2012), which reveals the difference in tem-  
 247 poral evolution of  $T_s$  between the cases of No-Humans and With-Humans.  
 248 The rate of change of  $T_s$  is given by an ordinary differential equation for Case

249 No-Humans:

$$\frac{dT_s}{dt} = \frac{\omega^{1/2}}{P} G(t) - \omega (T_s - T_b); \quad (4)$$

250 and for Case With-Humans:

$$\frac{d(T_s + \delta T_s)}{dt} = \frac{\omega^{1/2}}{P} (G(t) + \delta G(t)) - \omega (T_s + \delta T_s - (T_b + \delta T_b)), \quad (5)$$

251 where  $\omega$  is the principal diurnal frequency corresponding to the principal  
 252 Earth rotation frequency:  $\frac{1}{24 \times 3600} \text{ s}^{-1}$ ;  $P$  is the thermal inertia of the surface  
 253 material with units  $\text{J} \cdot \text{m}^{-2} \cdot \text{K}^{-1} \cdot \text{s}^{-1/2}$ , calculated from WUDAPT database.  
 254 The time evolution of  $\delta T_s$ , the resultant change in  $T_s$  due to perturbation by  
 255 AH, is given by Equation 5 - Equation 4 as:

$$\frac{d\delta T_s}{dt} = \frac{\omega^{1/2}}{P} (\delta G) - \omega (\delta T_s - \delta T_b), \quad (6)$$

256 where  $\delta G$ , the change to  $G$  caused by anthropogenic heat emissions, can be  
 257 substituted using the relation  $\delta G = \delta R_n - \delta H - \delta LE$ . Since the net short  
 258 wave radiation is not impacted by  $\delta T_s$  and  $\delta T_a$ ,  $\delta R_n$  is given by the change  
 259 in longwave radiation (LW) (i.e.,  $\delta R_n = \delta LW$ ), Equation 6 becomes

$$\frac{d\delta T_s}{dt} = \frac{\omega^{1/2}}{P} (\delta LW - \delta H - \delta LE) - \omega (\delta T_s - \delta T_b). \quad (7)$$

260 Applying the bulk parameterizations for sensible and latent heat fluxes  
 261 and a linearization of the Stefan-Boltzmann relation for the longwave radia-

tion, Equation 7 becomes

$$\frac{d\delta T_s}{d\tau} = - \left( 1 + \frac{r_a}{r_o} + \beta \frac{\delta}{\gamma} + \frac{r_a}{r_g} \right) \delta T_s + Q', \quad (8)$$

where  $\tau$  is  $t$  normalized by  $Pr_a/\sqrt{\omega}\rho c_p$  and the full expressions for  $\frac{r_a}{r_o}$ ,  $\beta \frac{\delta}{\gamma}$ ,  $\frac{r_a}{r_g}$  and  $Q'$  can be found in Appendix B. The negative coefficient on  $\delta T_s$  reflects the dissipative nature of the system towards the equilibrium state  $\delta T_s^*$  in the long time limit, which is  $\delta T_s^* = \frac{Q'}{1 + \frac{r_a}{r_o} + \beta \frac{\delta}{\gamma} + \frac{r_a}{r_g}}$ . The right hand side of Equation 8 indicates that the rate at which the system reaches its long time limit equilibrium is dependent on the four pathways, with the relative efficiencies of outgoing longwave radiation, latent heat flux and net rate change of heat storage at the surface relative to sensible heat flux given by  $\frac{r_a}{r_o}$ ,  $\beta \frac{\delta}{\gamma}$  and  $\frac{r_a}{r_g}$ , respectively. For example,  $\frac{r_a}{r_g}$  denotes the relative efficiency of  $G$  to  $H$  in dissipating energy, where  $r_a$  is the aerodynamic resistance and  $r_g$  is the surface conductive heat flux resistance given by:

$$r_g = \frac{\rho C_p}{P\sqrt{\omega}}. \quad (9)$$

It is worth noting that Oke et al. (2017, in Eq. 6.4)) defines the ratio between thermal inertia of the urban surface materials,  $\mu_g = P/\sqrt{2}$ , and that of the air,  $\mu_a$ , which indicates the sensible heat sharing between the urban surface materials and the turbulent air. However, here  $\frac{r_a}{r_g}$  signifies the relative importance of heat storage change compared to sensible heat flux in contributing to the observed  $T_s$  given the net available energy from both

280 radiation and anthropogenic heating. For the usual assumption underlying  
 281 the RS-SEB method to be valid, the term  $\frac{r_a}{r_g}$  should be much smaller than  
 282 one. A large value of  $\frac{r_a}{r_g}$  indicates that AH results in non-negligible change  
 283 in the net rate change of heat storage, invalidating this assumption. Thus,  
 284 we examine  $\frac{r_a}{r_g}$  across LCZ types 1-6 (Figure 4). Figure 4a compares  $\frac{r_a}{r_g}$  and  
 285 gridded AH normalized by the difference between maximum and minimum  
 286 values in each city (Chicago and Philadelphia as examples are shown in  
 287 Figure 4a). Relatively high values of  $\frac{r_a}{r_g}$  are found in areas with a relatively  
 288 low amplitude of AH, which usually overlap with the high-rise LCZ types. An  
 289 ensemble average of the LCZ-specific values of  $\frac{r_a}{r_g}$  and  $AH^{RS-SEB}$  across the  
 290 sample of cities is considered (Figure 4b), where for LCZ type  $i = 1 - 6$  they  
 291 are denoted as  $\overline{\frac{r_a}{r_g}_i}$  and  $\overline{AH_i^{RS-SEB}}$ . Figure 4b indicates distinctly opposite  
 292 trends across the LCZs. Details of  $\frac{r_a}{r_g}_i$  are further illustrated in Table 2 for  
 293 each selected city. Generally, for a given degree of urban surface compactness  
 294 summarized by the LCZ types (e.g., compact high, medium and low-rise  
 295 buildings in LCZs 1-3, respectively),  $\frac{r_a}{r_g}$  decreases with decreasing building  
 296 height, in contrast to variation of AH across the LCZ types. The intra-city  
 297 differences are mainly due to thermal inertia  $P$  (e.g. Values of  $P$  in LCZ 4-6  
 298 are  $1.04 \times 10^3$ ,  $0.98 \times 10^3$  and  $0.89 \times 10^3 \text{ J}\cdot\text{m}^{-2}\cdot\text{K}^{-1}\cdot\text{s}^{-1/2}$ , respectively), while  
 299 the inter-city differences can be attributed to different aerodynamic resistance  
 300  $r_a$ . For example,  $r_a$  in Chicago ranges from 20-30  $\text{s}\cdot\text{m}^{-1}$  in the selected  
 301 day; while in Houston,  $r_a$  ranges from 60-70  $\text{s}\cdot\text{m}^{-1}$ . These results indicate  
 302 that for urban surfaces characterized by high and dense building fractions,

303 heat storage is a significant pathway for anthropogenic heat. Therefore, the  
304 key assumption that  $AH \approx H_a$  in the RS-SEB method is not applicable in  
305 urban land surfaces where the anthropogenic energy source is more effectively  
306 partitioned into  $G$ . A simple parameterization for  $G$  as a fraction of  $R_n$  will  
307 not account for the partitioned AH, and therefore can lead to consistent  
308 underestimation of AH and the results should be regarded as AH partitioned  
into sensible heat.

Table 2: Means of  $r_a/r_g$  in selected LCZs

ineB3	LCZ 1	LCZ 2	LCZ 3	LCZ 4	LCZ 5	LCZ 6
ineB3 CHI	0.146	0.133	0.084	0.121	0.113	0.078
DC	0.158	0.147	0.091	/	0.128	0.089
HOU	0.369	0.351	/	0.383	0.323	0.184
LA	0.223	/	0.129	/	0.164	0.110
PHL	0.280	0.229	0.174	0.232	/	0.150
PHX	0.214	/	0.118	0.217	0.165	0.114
ineB3						

309

## 310 4. Conclusion

311 Remote sensing is an important emerging technique in AH quantification  
312 and estimation of urban surface energy energy fluxes (Chrysoulakis et al.,  
313 2018). The effects of AH intertwined with other components of the SEB  
314 impose significant challenges to quantify changes in the SEB due to anthro-  
315 pogenic energy emissions (i.e., the urban function)(Oke et al., 2017). The  
316 non-negligible change of heat storage term in the SEB caused by addition  
317 of AH becomes important on sub-daily time scales, which critically impact

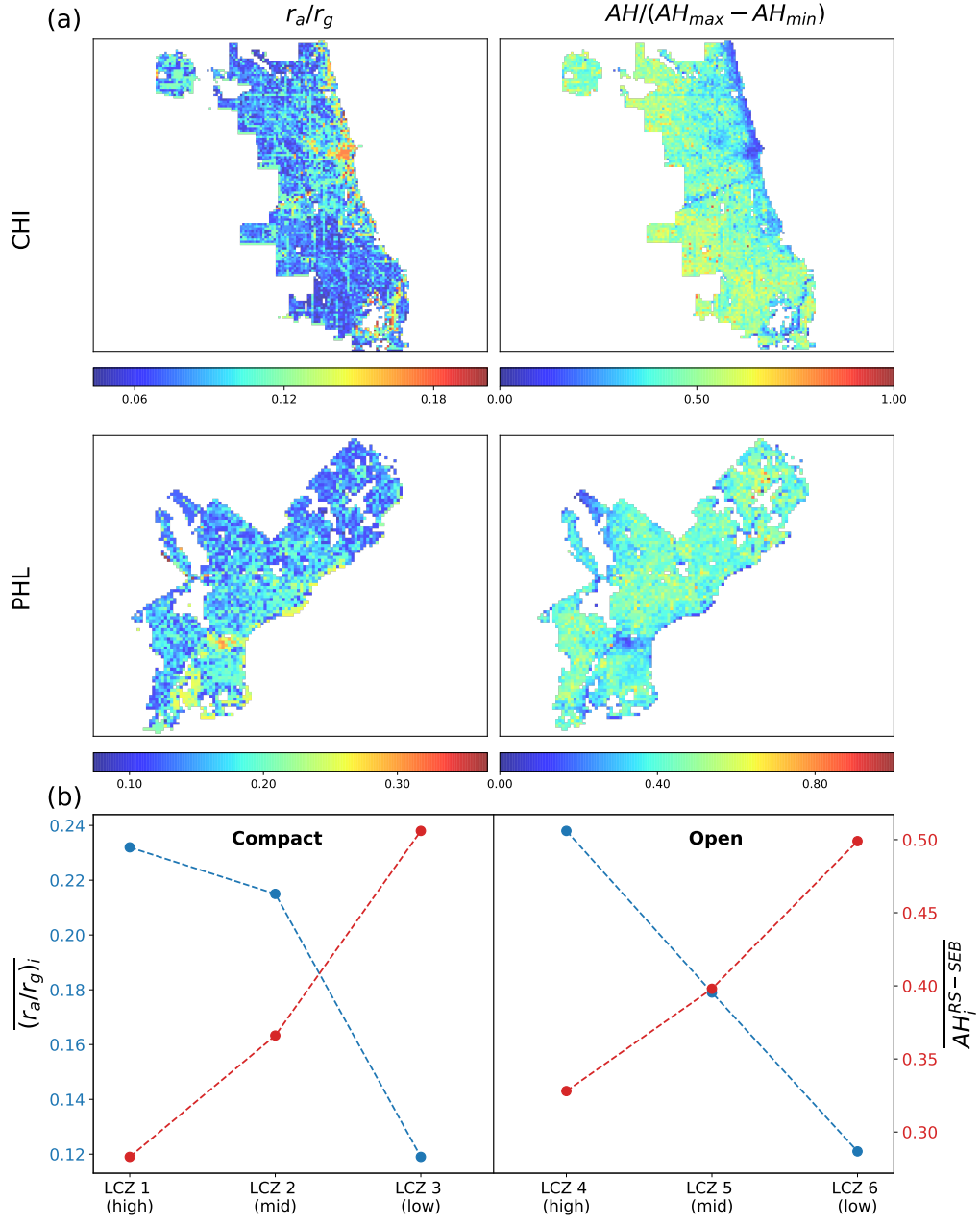


Figure 4: (a) Left column: Energy partitioning efficiencies of heat storage relative to the sensible heat flux in Chicago (CHI) and Philadelphia (PHL). Right column: pixel-wise AH normalized with the difference between maximum AH and minimum AH in respective cities. (b)  $\overline{(r_a/r_g)}_i$  and  $\overline{AH_i^{RS-SEB}}_i$ :  $\overline{(r_a/r_g)}_i$  and  $\overline{AH_i^{RS-SEB}}_i$  for LCZ type  $i$ , where  $i=1, 2, 3, 4, 5, 6$ , averaged over the ensemble of cities.

the quality and reliability of AH estimated by the RS-SEB method. The implication of AH-induced change in heat storage is accessed in this study using satellite observations of the land surface temperature combined with analytical investigation under the LCZ classification framework.

Leveraging level-zero data from the WUDAPT, we estimated LCZ-type-specific AH in six US cities from Landsat 8. The resultant maps of AH and the corresponding statistics indicate that LCZs with high-rise buildings (i.e., LCZ 1 and 4) are more inclined to have lower values of AH than those characterized by low-rise buildings (i.e., LCZ 3 and 6), regardless of the built-up density, which is opposite to the patterns found in WUDAPT reference values adopted from the LCZ classification criterion (Stewart and Oke, 2012). The discrepancy highlights the importance of AH-induced change in heat storage, especially in LCZs with high volume of built materials per unit area. Thus, the assumption of the RS-SEB method, which proposes AH does not alter other components of the SEB except for the sensible heat flux (Kato and Yamaguchi, 2005), can be violated in these LCZs. This implies that on sub-diurnal time scales, the high thermal inertia of building materials causes high heat storage, thus the time lag between building energy consumption and surface temperature increment that is detectable by the remote sensing instruments can significantly deteriorate the reliability of AH computed from the RS-SEB method. It is also noteworthy that the inventory-based method can be affected by this phenomena, since the time lag between energy consumption and conversion to anthropogenic sensible heat flux is neglected

341 (Sailor, 2011), introducing uncertainty in deriving the sub-diurnal tempo-  
342 ral profile of AH. Subsequent stability analysis of the SEB equation indicates  
343 that the efficiency of energy partitioning between sensible heat and heat stor-  
344 age given by the ratio of the resistance factors ( $\frac{r_a}{r_g}$ ) is critical in identifying  
345 areas prone to errors in AH using the RS-SEB method.

346 In light of the emergence of databases for urban LULC representations  
347 (e.g., the WUDAPT (Ching et al., 2018)) and the promising results of using  
348 satellite observations to quantify urban surface fluxes (Chrysoulakis et al.,  
349 2018), there is a great potential for integrating earth observations into quan-  
350 tification of AH with a unified platform of urban LULC database. With  
351 relatively straightforward data acquisition, the RS-SEB method can poten-  
352 tially be extended to cities worldwide and coupled with numerical weather  
353 and climate models for city-specific AH profiles. However, the significant im-  
354 pact of AH on heat storage is a key determining factor for its applicability,  
355 especially in urban core areas (e.g. LCZ 1 and LCZ 4) with high ratio of  $\frac{r_a}{r_g}$ .  
356 It is recommended that for neighborhoods with a high ratio of  $\frac{r_a}{r_g}$ , alterna-  
357 tive methods to estimate AH such as the inventory method may complement  
358 the RS-SEB method. Although overcoming the deficiency of this method  
359 is beyond the scope of this study, future research on remote-sensing-based  
360 quantification of AH will benefit from improving the representation of the  
361 heat storage term (Lindberg et al., 2020; Hrisko et al., 2021) when applying  
362 the RS-SEB method. In addition, it implies that AH-induced change in other  
363 components of the urban SEB should be cautiously assessed, especially the



time-lag between AH and sensible heat for evaluating the impact of AH on  
time-dependent urban climate phenomena such as precipitation (Holst et al.,  
2016; Feng et al., 2012; Nie et al., 2017; Zhang et al., 2018).

### **Description of author’s responsibilities**

Zhou Yu: Formal analysis, Method, Writing- Original draft, review and  
editing; Leiqiu Hu: Method, Writing - Review and editing; Ting Sun: Method,  
Writing -Review and editing; John Albertson: Method, Writing -Review and  
editing; Qi Li: Conceptualization, Method, Writing - Original draft, review  
and editing.

### **Acknowledgement**

There are no financial conflicts of interests for any author. This work  
is funded by NASA’s Interdisciplinary Research in Earth Science (IDS) pro-  
gram (80NSSC20K1263). All data used in this study are publicly available.  
Landsat 8 products can be freely ordered through United States Geological  
Survey (USGS): <https://earthexplorer.usgs.gov/>. 1-min weather sta-  
tion data are provided by the Automated Surface Observing System (ASOS):  
<ftp://ftp.ncdc.noaa.gov/pub/data/asos-onemin/>. Information regard-  
ing local climate zone (LCZ) classification maps and related surface descrip-  
tors are available from the World Urban Database and Access Portal Tools  
(WUDAPT) level 0 database: <http://www.wudapt.org/>.

## 384 **Appendix A. AH quantification using the RS-SEB method**

385 First, all data from external sources are listed here:

386 Satellite products: Landsat 8 level 1 and level 2 (surface reflectance)  
387 images at Chicago (20170915), District of Columbia (20170923), Houston  
388 (20170406), Los Angeles (20171015), Philadelphia (20171002) and Phoenix  
389 (20171003).

390 Meteorological observations: wind speed and air temperature from ASOS  
391 1-min data corresponding to the time of satellite passing. The observation  
392 site is the local airport at each city.

393 Atmospheric correction parameters (atmospheric transmission, effective  
394 bandpass upwelling radiance and effective bandpass downwelling radiance)  
395 required in the retrieval of land surface temperature are calculated by a tool  
396 from NASA ([atmcorr.gsfc.nasa.gov/](http://atmcorr.gsfc.nasa.gov/)), using the mid-latitude summer mode.

397 LCZ-specific urban canopy parameters (e.g. zero-plane displacement height,  
398 plan area density, etc.) are from the level 0 data provided by the World Urban  
399 Database and Access Portal Tools (WUDAPT).

400 We adopt the framework of Kato and Yamaguchi (2005) to estimate AH,  
401 which is briefly outlined here. First, sensible heat flux due to radiant heat  
402 balance is denoted as  $H_n$ , which can be calculated as the residual of the SEB  
403 equation where  $R_n$  the net radiation is the energy input:

$$H_n = R_n - G - LE \quad (\text{A.1})$$

Secondly, both  $H_n$  and the increase in sensible heat flux due to AH, which is denoted as  $H_{as}$ , contribute to the total sensible heat flux  $H$ :

$$H_n + H_{as} = H \quad (\text{A.2})$$

Therefore,  $H_{as} = R_n - G - LE - H$ , where  $R_n$ ,  $G$ ,  $LE$  and  $H$  can be calculated from parameterizations using remotely-sensed surface temperature. Although  $H_{as}$  is not equivalent to AH, under their assumption that the influence of temperature rise (i.e., increase in both air and surface temperatures due to AH) is only non-negligible for sensible heat in this framework,  $H_{as} = AH$ . Next we outline how each component in the SEB equation is computed. In general, procedures similar to their study are adopted and whenever appropriate, adaptations of the method to urban land use data provided by the WUDAPT will be described.

#### *Appendix A.1. Net Radiation ( $R_n$ )*

$$\begin{aligned} R_n &= R_{L\downarrow} - R_{L\uparrow} + R_{S\downarrow} - R_{S\uparrow} \\ &= \varepsilon_a \sigma T_a^4 - [\varepsilon_s \sigma T_s^4 + (1 - \varepsilon_s) R_{L\downarrow}] + (1 - \alpha) R_{S\downarrow} \\ &= \varepsilon_s \varepsilon_a \sigma T_a^4 - \varepsilon_s \sigma T_s^4 + (1 - \alpha) G_{SC} \cos \theta d_r \tau \end{aligned} \quad (\text{A.3})$$

where  $\varepsilon_s$  is surface emissivity and  $\varepsilon_a$  is atmospheric emissivity.  $T_s$  and  $T_a$  stand for surface temperature and air temperature (K).  $T_a$  obtained from the

418 local airport in each city is assumed to be representative of the entire study  
 419 area. This simplification is justified because as reported in a study (Craw-  
 420 ford et al. 2018) that estimates heat flux from remotely-sensed land surface  
 421 temperautre, unevenly distributed air temperature in cities and non-uniform  
 422 installation of sensors can introduce uncertainty in spatial interpolation of  
 423 the air temperature. Furthermore, the spatial variability of air temperature  
 424 above the urban canopy layer is much less than that of remotely-sensed land  
 425 surface temperature. Therefore, they opted for using a single reliable air  
 426 temperature measurement for flux estimation.  $\alpha$  is surface albedo, calcu-  
 427 lated on top of band-wise surface reflectance (Wang et al. 2016).  $\sigma$  is the  
 428 Stefan-Boltzmann Constant ( $5.67 \times 10^{-8} \text{ W} \cdot \text{m}^{-2} \cdot \text{K}^{-4}$ ).  $G_{SC}$  is the Solar  
 429 Constant:  $1367 \text{ W} \cdot \text{m}^{-2}$ .  $\theta$  is the zenith angle of observation.  $d_r$  is the Earth-  
 430 Sun distance.  $\theta$  and  $d_r$  are included in the Landsat 8 level 1 product.  $\tau$   
 431 is the air transmissivity provided by the Atmospheric Correction Parameter  
 432 Calculator of NASA.

#### 433 *Appendix A.2. Ground Heat (G)*

434 Ground heat flux can be considered to be proportional to net radiation:

$$G = C_g R_n \quad (\text{A.4})$$

435 where  $C_g$  is the determining coefficient. For urban lands, a universal value  
 436 of 0.7 is used (Kato and Yamaguchi, 2005).

437 *Appendix A.3. Sensible Heat ( $H$ )*

$$H = \rho C_p \frac{T_s - T_a}{r_a} \quad (\text{A.5})$$

438 where  $\rho$  is air density and  $C_p$  is specific heat capacity of air. The land surface  
 439 temperature  $T_s$ , is an alternative of aerodynamic temperature ( $T_{aero}$ ) for its  
 440 easier access.  $r_a$  refers to aerodynamic resistance.

441 A pixel-wise modeling of  $r_a$  is introduced on three parameters below in-  
 442 stead of taking rule-of-thumb values against different land-use types:

443 • **zero-plane displacement height  $d$**

444 This is defined as the height at which zero wind speed is achieved due  
 445 to the appearance of obstacles like buildings, trees, etc. It is approxi-  
 446 mately two thirds of the height of overlying obstacles on natural sur-  
 447 faces. Combining the model from wind-tunnel experiments (Macdonald  
 448 et al., 1998) and urban morphological data, we specify its calculation  
 449 on every individual urban pixel as below:

$$\frac{d}{H} = 1 + A^{-\lambda_p}(\lambda_p - 1) \quad (\text{A.6})$$

450 where  $H$  is the mean height of obstacles, replaced by mean building  
 451 height within a grid.  $\lambda_p$  is the plan area density.  $A$  is a simulated  
 452 constant, which is 4.43 for staggered obstruction arrays under urban  
 453 settings (Macdonald et al. 1998). The values of  $H$  and  $\lambda_p$  are obtained

454 from the level 0 data in WUDAPT and Oke et al. (2017), respectively  
 455 (Table A.3).

Table A.3:  $H$  and  $\lambda_p$  values from WUDAPT

ineB3	LCZ 1	LCZ 2	LCZ 3	LCZ 4	LCZ 5	LCZ 6	LCZ 7	LCZ 8	LCZ 9	LCZ 10
ineB3 $H$	37.5	17.5	6.5	37.5	17.5	6.5	3	6.5	6.5	10
$\lambda_p$	0.5	0.55	0.55	0.3	0.3	0.3	0.75	0.4	0.15	0.25
ineB3										

### 456 *Appendix A.3.1. Wind speed $u_z$*

457 Wind speed data are from ASOS and nearby automatic weather sta-  
 458 tions from Weather Underground (wunderground.com) serve as back-  
 459 ups only if data of certain days are missing. Wind speed at each urban  
 460 pixel is extrapolated from the weather station value using the reference  
 461 height scaling method (Crawford et al., 2018; Wieringa, 1986), where a  
 462 neutral stability is assumed in this study. This reference height scaling  
 463 method shown in equations below first interpolates the measured wind  
 464 speed  $U$  to a reference height  $z_{ref}$  to obtain  $U_{ref}$ , where  $z_{ref}$  is assumed  
 465 to be 200 m, indicating a level high enough for the logarithmic wind  
 466 profile to be valid. Then,  $U_{ref}$  is interpolated to 1.5 times the height  
 467 of mean obstacle (building) height  $H$  at each urban grid to obtain  $u_z$ ,  
 468 such that bulk aerodynamic method for turbulent fluxes parameteriza-  
 469 tion are subsequently applied uniformly across all urban grids at  $1.5H$ ,  
 470 which is regarded as near top of the urban roughness sublayer, where  
 471 the inertial sublayer with a logarithmic wind profile starts. Although

472 the demarcation of inertial sublayer can vary depending on the under-  
 473 lying surface roughness,  $1.5H$  seems to be reasonable in computing the  
 474 aerodynamic resistance as shown in Crawford et al. (2018).

$$U_{ref} = U_{obs} \frac{\ln\left(\frac{z_{ref}-d_{obs}}{z_{0,obs}}\right)}{\ln\left(\frac{z_{m,obs}-d_{obs}}{z_{0,obs}}\right)} \quad (\text{A.7})$$

$$u_z = U_{ref} \frac{\ln\left(\frac{z_m-d}{z_{0m}}\right)}{\ln\left(\frac{z_{ref}-d_{obs}}{z_{0,obs}}\right)} \quad (\text{A.8})$$

476  $d_{obs}$  is the displacement height at the observational site;  $z_{m,obs}$  and  $z_{0,obs}$   
 477 are the height of wind (momentum) sensor and the roughness length for  
 478 momentum at the observational site, respectively. The necessary urban  
 479 parameters for the above interpolation at local airports can be obtained  
 480 through Davenport classification of effective terrain roughness (Stewart  
 481 and Oke, 2012; Davenport et al., 2000) and WUDAPT classification of  
 482 local climates. Each observational site at the local airport is located  
 483 in the WUDAPT LCZ classification map, where LCZs 8 and 10 are  
 484 found as the dominant types for sites. Thus,  $H = 10$  m,  $\lambda_p = 0.55$ , and  
 485 the computed displacement height  $d_{obs} = 8.0$  m. Furthermore, building  
 486 layouts at each local airport are visually inspected in the Google Map,  
 487 which then are classified as 'Rough' in Davenport classes with  $z_{0,obs} =$   
 488  $0.25$  m according to the tabulated value.

Appendix A.3.2. roughness length for momentum ( $z_{0m}$ ) and heat ( $z_{0h}$ )

First, the roughness length ( $z_{0m}$ ) at each pixel is computed following the relation  $z_{0m} = 1/10H$  as implemented in Grimmond and Oke (1999). Second, the heat roughness length ( $z_{0h}$ ) is computed using the  $kB^{-1}$  relation (Crawford et al., 2018; Li et al., 2020):

$$\ln \frac{z_{0m}}{z_{0h}} = kB^{-1}, \quad (\text{A.9})$$

in which

$$kB^{-1} = \beta(Re_*)^{0.25} - 2.0,$$

follows the theoretical derivation in (Brutsaert, 1982), where  $Re_*$ , the roughness Reynolds number is  $\frac{z_{0m}u_*}{\nu}$ ,  $u_*$  being the friction velocity and  $\nu$  being the kinematic viscosity ( $1.46 \times 10^{-5} \text{ m}^2 \text{ s}^{-1}$ ). The empirical constant  $\beta$  varies according to different surface types (Kanda et al., 2007), here it is modeled with respect to vegetation cover (Crawford et al., 2018), given by  $\beta = 0.87e^{-0.997FVC}$ , where  $FVC$  is the fractional vegetation cover.

The equation for the bulk aerodynamic resistance  $r_a$  is :

$$r_a = \frac{\ln \left( \frac{z_m - d}{z_{0m}} \right) \ln \left( \frac{z_m - d}{z_{0h}} \right)}{k^2 u_z}. \quad (\text{A.10})$$

where  $z_m$  equals to 1.5 times mean building height, at which height bulk aerodynamic method for turbulent fluxes parameterization applies.



504 *Appendix A.4. Latent Heat (LE)*

$$LE = \frac{\rho C_p}{\gamma} \frac{e_s - e_a}{r_s + r_a}, \quad (\text{A.11})$$

505 where  $\gamma$  is the psychrometric constant (approximately  $0.66 \text{ hPa} \cdot \text{K}^{-1}$ );  $e_s$  is  
 506 saturated water vapor pressure and  $e_a$  is actual water vapor pressure (hPa);  
 507  $r_s$  is the stomatal resistance ( $\text{s} \cdot \text{m}^{-1}$ ). For typical urban area, a reference  
 508 value of 200 for  $r_s$  is used (Zhang et al., 2003).

509 **Appendix B. Stability analysis of the SEB using the force-restore**  
 510 **approach**

511 Details of stability analysis of the SEB equation where the force-restore  
 512 approach is adopted are outlined in this section. In subsequent derivations,  
 513 the symbol  $\delta$  indicates the change of some quantity of interest caused by  
 514 anthropogenic heat.

515 Change of net longwave radiation is comprised of the change of incoming  
 516 longwave energy with its outgoing counterpart subtracted:

$$\begin{aligned} \delta LW_{\downarrow} &= \varepsilon_a \sigma (T_a + \delta T_a)^4 - \varepsilon_a \sigma T_a^4 \\ &\approx \varepsilon_a \sigma T_a^4 + 4\varepsilon_a \sigma \delta T_a T_a^3 - \varepsilon_a \sigma T_a^4 \\ &= 4\varepsilon_a \sigma \delta T_a T_a^3 \end{aligned} \quad (\text{B.1})$$

$$\begin{aligned}
\delta LW_{\uparrow} &= \varepsilon_s \sigma (T_s + \delta T_s)^4 - \varepsilon_s \sigma T_s^4 + (1 - \varepsilon_s) \delta LW_{\downarrow} \\
&\approx \varepsilon_s \sigma T_s^4 + 4\varepsilon_s \sigma \delta T_s T_s^3 - \varepsilon_s \sigma T_s^4 + (1 - \varepsilon_s) \delta LW_{\downarrow} \quad (\text{B.2}) \\
&= 4\varepsilon_s \sigma \delta T_s T_s^3 + 4(1 - \varepsilon_s) \varepsilon_a \sigma \delta T_a T_a^3
\end{aligned}$$

$$\delta LW = \delta LW_{\downarrow} - \delta LW_{\uparrow} = 4\varepsilon_s \varepsilon_a \sigma \delta T_a T_a^3 - 4\varepsilon_s \sigma \delta T_s T_s^3 \quad (\text{B.3})$$

517 where  $\varepsilon_s$  and  $\varepsilon_a$  are surface and air emissivity, respectively;  $\sigma$  is the Stefan-  
518 Boltzmann Constant;  $T_a$  and  $T_s$  are air temperature and surface temperature  
519 (K).

520 Change of  $\delta H$  is attributed to the change of surface temperature and air  
521 temperature:

$$\begin{aligned}
\delta H &= \rho C_p \frac{(T_s + \delta T_s) - (T_a + \delta T_a)}{r_a} - \rho C_p \frac{T_s - T_a}{r_a} \\
&= \rho C_p \frac{\delta T_s}{r_a} - \rho C_p \frac{\delta T_a}{r_a} \quad (\text{B.4})
\end{aligned}$$

522 where  $r_a$  is the aerodynamic resistance ( $\text{s}\cdot\text{m}^{-1}$ );  $\rho$  is the density of air ( $\text{g}\cdot\text{m}^{-3}$ );  
523  $C_p$  is specific heat capacity of air at a constant pressure ( $\text{J}\cdot\text{g}^{-1}\cdot\text{K}^{-1}$ ).

524 The difference of latent heat is calculated as below, assuming little influ-

ence of human activities on actual air humidity ( $q_a$ ):

$$\begin{aligned}
\delta LE &= \frac{\beta \rho L}{r_a} (q_s^*(T_s + \delta T_s) - q_a) - \frac{\beta \rho L}{r_a} (q_s^*(T_s) - q_a) \\
&= \frac{\beta \rho L}{r_a} (q_s^*(T_s + \delta T_s) - q_s^*(T_s)) \\
&\approx \frac{\beta \rho L}{r_a} \left. \frac{\partial q_s^*}{\partial T_s} \right|_{T_s} \delta T_s
\end{aligned} \tag{B.5}$$

where  $\beta$  is a parameter related to moisture availability,  $L$  is the specific latent heat of vaporization and  $q_s^*/q_a$  represents the function for saturated specific humidity/air humidity at given temperature.

Substitute Equation B.5 and Equation B.4 in the main text with the above items:

$$\begin{aligned}
\frac{d\delta T_s}{dt} &= \frac{\omega^{1/2}}{P} \left( 4\varepsilon_s \varepsilon_a \sigma \delta T_a T_a^3 - 4\varepsilon_s \sigma \delta T_s T_s^3 - \rho C_p \frac{\delta T_s}{r_a} + \rho C_p \frac{\delta T_a}{r_a} - \frac{\beta \rho L}{r_a} \left. \frac{\partial q_s^*}{\partial T_s} \right|_{T_s} \delta T_s \right) \\
&\quad - \omega (\delta T_s - \delta T_b) \\
&= \frac{\omega^{1/2}}{P} \left( -4\varepsilon_s \sigma T_s^3 - \frac{\rho C_p}{r_a} - \frac{\beta \rho L}{r_a} \left. \frac{\partial q_s^*}{\partial T_s} \right|_{T_s} - \omega \right) \delta T_s \\
&\quad + \frac{\omega^{1/2}}{P} \rho C_p \frac{\delta T_a}{r_a} + 4 \frac{\omega^{1/2}}{P} \varepsilon_s \varepsilon_a \sigma \delta T_a T_a^3 + \omega \delta T_b
\end{aligned} \tag{B.6}$$

After rearrangement of Eq. B.6, where:

$$\tau = \frac{\omega^{1/2}}{P} \frac{\rho C_p}{r_a} t$$

$$r_o = \frac{\rho C_p}{4\varepsilon_s \sigma T_s^3}$$

$$r_g = \frac{\rho C_p}{P\omega^{1/2}}$$

$$\delta_q = \frac{dq_s^*}{dT_s}$$

$$\gamma = \frac{\omega^{1/2} C_p}{L}$$

$$Q' = \frac{\rho C_p}{r_a} (4\varepsilon_s \varepsilon_a \sigma T_a^3 \delta T_a + \frac{\omega^{1/2}}{P} \delta T_a + P\omega^{1/2} \delta T_b)$$

531 We get:

$$\frac{d\delta T_s}{d\tau} = - \left( 1 + \frac{r_a}{r_o} + \beta \frac{\delta_q}{\gamma} + \frac{r_a}{r_g} \right) \delta T_s + Q' \quad (\text{B.7})$$

532 Solution to Eq. B.7 is:

$$\delta T_s(\tau) = c_1 e^{-\frac{r_a}{r_o}\tau} e^{-\tau} e^{-\beta \frac{\delta}{\gamma}\tau} e^{-\frac{r_a}{r_g}\tau} + \frac{Q'}{\frac{r_a}{r_g} + 1 + \beta \frac{\delta}{\gamma} + \frac{r_a}{r_g}} \quad (\text{B.8})$$

533 where  $c_1$  is a constant.

### 534 **Appendix C. Computation of $r_a/r_g$**

535  $r_a$  is obtained as aforementioned in the estimation of sensible heat flux.

536 The LCZ-specific  $r_g$  is given by  $P\sqrt{\omega}$ , where  $\omega$  is a frequency parameter

537 here at the diurnal scale:  $\frac{1}{24 \times 3600} \text{ s}^{-1}$  and  $P$  is thermal inertia ( $\text{J} \cdot \text{m}^{-2} \cdot \text{K}^{-1} \cdot \text{s}^{-1/2}$ ):

$$P = \sqrt{\frac{Ck}{2}} \quad (\text{C.1})$$

538 where  $C$  is heat capacity ( $\text{J} \cdot \text{m}^{-3} \cdot \text{K}^{-1}$ ) and  $k$  is thermal conductivity ( $\text{J} \cdot$   
539  $\text{m}^{-1} \cdot \text{s}^{-1} \cdot \text{K}^{-1}$ ). Here  $P$  is defined with a prefactor 2 following that in Bateni

et al. (2012), which is different from that without the prefactor 2 in Goward (1981); Oke et al. (2017); Wang et al. (2010). Nevertheless, difference in the definition of thermal inertia does not change the variation of  $\frac{r_a}{r_g}$  the LCZs.

The retrieval of thermal inertia ( $P$ ) is based on the heat capacity ( $C$ ) and thermal conductivity ( $k$ ) data from LCZ look-up tables. Such thermal properties for three elements (roof, wall and road) constituting urban surfaces are provided across ten LCZ types (Table C.4). In addition, such properties for moist soil (in non built-up area) are from Bateni and Entekhabi (2012). The average water content of clay and sand is assumed to be 0.27, based on which volumetric heat capacity is  $2.6 \times 10^6 (Jm^{-3}K^{-1})$  and heat conductivity is  $1.35 (Wm^{-1}K^{-1})$ . A representative thermal inertia is calculated from a weighted assignment of thermal inertia values of the three major urban compositions. The weight for each LCZ type is decided according to the ratio of surface area between the roof, wall, road and soil (buildings are simplified as cuboids with square basis and four-sided walls). For example, building fraction in LCZ 1 is 50%, which could be approximated to the roof fraction. Consequently, due to the full urbanization in this LCZ class, road surfaces account for the rest of 50%. Meanwhile, the total wall surfaces are ten times to the roof surface, given average building height is 37.5 meters and average building width is 15 meters ( $\frac{15 \times 37.5 \times 4}{15 \times 15} = 10$ ). As a result, the ratios among road, roof, wall and soil are 1 : 1 : 10 : 0, based on which those weighted thermal parameters are calculated.

Table C.4: Thermal properties (heat capacity  $C_i$  in  $Jm^{-3}K^{-1} \times 10^6$  and thermal conductivity  $k_i$  in  $Jm^{-1}s^{-1}K^{-1}$ ) and fraction of urban surface type  $i$  across LCZs, where  $i$  refers to roof, wall, road and soil.

ineB3	$C_{roof}$	$C_{wall}$	$C_{road}$	$k_{roof}$	$k_{wall}$	$k_{road}$	roof (%)	wall (%)	road (%)	soil (%)
ineB3 LCZ 1	1.8	1.8	1.75	1.25	1.09	0.77	8.33	83.33	8.33	0
LCZ 2	1.8	2	1.5	1.25	1.45	0.62	17.19	68.75	12.5	1.56
LCZ 3	1.44	2.05	1.63	1	1.25	0.69	21.24	61.39	13.51	3.86
LCZ 4	1.8	2	1.54	1.25	1.45	0.64	12.45	58.51	14.52	14.52
LCZ 5	1.8	2	1.5	1.25	1.45	0.62	16.30	45.65	21.74	16.30
LCZ 6	1.44	2.05	1.47	1	1.25	0.6	17.24	42.53	20.11	20.11
LCZ 7	2	0.72	1.38	2	0.5	0.51	32.75	56.33	4.37	6.55
LCZ 8	1.8	1.8	1.8	1.25	1.25	0.8	29.41	26.47	33.09	11.03
LCZ 9	1.44	2.56	1.37	1	1	0.55	10.79	28.06	10.79	50.36
LCZ 10	2	1.59	1.49	2	1.33	0.61	17.61	29.58	21.13	31.69
ineB3										

## References

- A. K. Quah, M. Roth, Diurnal and weekly variation of anthropogenic heat emissions in a tropical city, singapore, *Atmospheric Environment* 46 (2012) 92–103.
- G. Pigeon, D. Legain, P. Durand, V. Masson, Anthropogenic heat release in an old european agglomeration (toulouse, france), *International Journal of Climatology: A Journal of the Royal Meteorological Society* 27 (2007) 1969–1981.
- D. J. Sailor, L. Lu, A top-down methodology for developing diurnal and seasonal anthropogenic heating profiles for urban areas, *Atmospheric environment* 38 (2004) 2737–2748.
- L. Allen, F. Lindberg, C. Grimmond, Global to city scale urban anthro-

574 pogenic heat flux: model and variability, *International Journal of Clima-*  
 575 *tology* 31 (2011) 1990–2005.

576 S. Bohnenstengel, I. Hamilton, M. Davies, S. Belcher, Impact of anthro-  
 577 pogenic heat emissions on london’s temperatures, *Quarterly Journal of*  
 578 *the Royal Meteorological Society* 140 (2014) 687–698.

579 W. T. Chow, F. Salamanca, M. Georgescu, A. Mahalov, J. M. Milne, B. L.  
 580 Ruddell, A multi-method and multi-scale approach for estimating city-  
 581 wide anthropogenic heat fluxes, *Atmospheric environment* 99 (2014) 64–  
 582 76.

583 C. C. Holst, C.-Y. Tam, J. C. Chan, Sensitivity of urban rainfall to anthro-  
 584 pogenic heat flux: a numerical experiment, *Geophysical Research Letters*  
 585 43 (2016) 2240–2248.

586 J.-M. Feng, Y.-L. Wang, Z.-G. Ma, Y.-H. Liu, Simulating the regional im-  
 587 pacts of urbanization and anthropogenic heat release on climate across  
 588 china, *Journal of Climate* 25 (2012) 7187–7203.

589 W. Nie, B. F. Zaitchik, G. Ni, T. Sun, Impacts of anthropogenic heat on  
 590 summertime rainfall in beijing, *Journal of Hydrometeorology* 18 (2017)  
 591 693–712.

592 W. Zhang, G. Villarini, G. A. Vecchi, J. A. Smith, Urbanization exacerbated  
 593 the rainfall and flooding caused by hurricane harvey in houston, *Nature*  
 594 563 (2018) 384–388.

595 M. Iamarino, S. Beevers, C. Grimmond, High-resolution (space, time) an-  
 596 thropogenic heat emissions: London 1970–2025, *International Journal of*  
 597 *Climatology* 32 (2012) 1754–1767.

598 D. J. Sailor, A review of methods for estimating anthropogenic heat and  
 599 moisture emissions in the urban environment, *International journal of*  
 600 *climatology* 31 (2011) 189–199.

601 Y. Dong, A. Varquez, M. Kanda, Global anthropogenic heat flux database  
 602 with high spatial resolution, *Atmospheric Environment* 150 (2017) 276–  
 603 294.

604 B. Offerle, C. S. Grimmond, K. Fortuniak, Heat storage and anthropogenic  
 605 heat flux in relation to the energy balance of a central European city centre,  
 606 *International Journal of Climatology* 25 (2005) 1405–1419.

607 P. Zhang, C. Yuan, Q. Sun, A. Liu, S. You, X. Li, Y. Zhang, X. Jiao, D. Sun,  
 608 M. Sun, et al., Satellite-based detection and characterization of indus-  
 609 trial heat sources in china, *Environmental science & technology* 53 (2019)  
 610 11031–11042.

611 N. Chrysoulakis, S. Grimmond, C. Feigenwinter, F. Lindberg, J.-P. Gastellu-  
 612 Etchegorry, M. Marconcini, Z. Mitraka, S. Stagakis, B. Crawford, F. Olof-  
 613 son, et al., Urban energy exchanges monitoring from space, *Scientific*  
 614 *reports* 8 (2018) 1–8.



- 615 S. Kato, Y. Yamaguchi, Analysis of urban heat-island effect using aster  
616 and etm+ data: Separation of anthropogenic heat discharge and natural  
617 heat radiation from sensible heat flux, Remote Sensing of Environment 99  
618 (2005) 44–54.
- 619 Y. Zhou, Q. Weng, K. R. Gurney, Y. Shuai, X. Hu, Estimation of the relation-  
620 ship between remotely sensed anthropogenic heat discharge and building  
621 energy use, ISPRS Journal of Photogrammetry and Remote Sensing 67  
622 (2012) 65–72.
- 623 M. S. Wong, J. Yang, J. Nichol, Q. Weng, M. Menenti, P. W. Chan, Modeling  
624 of anthropogenic heat flux using hj-1b chinese small satellite image: A  
625 study of heterogeneous urbanized areas in hong kong, IEEE geoscience  
626 and remote sensing letters 12 (2015) 1466–1470.
- 627 T. Oke, G. Mills, A. Christen, J. A. Voogt, Urban climates, Cambridge  
628 University Press, 2017.
- 629 I. D. Stewart, T. R. Oke, Local climate zones for urban temperature studies,  
630 Bulletin of the American Meteorological Society 93 (2012) 1879–1900.
- 631 J. Ching, G. Mills, B. Bechtel, L. See, J. Feddema, X. Wang, C. Ren,  
632 O. Brousse, A. Martilli, M. Neophytou, et al., Wudapt: An urban weather,  
633 climate, and environmental modeling infrastructure for the anthropocene,  
634 Bulletin of the American Meteorological Society 99 (2018) 1907–1924.

635 S. M. Roberts, T. R. Oke, C. Grimmond, J. A. Voogt, Comparison of four  
636 methods to estimate urban heat storage, *Journal of applied meteorology*  
637 and climatology 45 (2006) 1766–1781.

638 S. Hanna, E. Marciotto, R. Britter, Urban energy fluxes in built-up downtown  
639 areas and variations across the urban area, for use in dispersion models,  
640 *Journal of applied meteorology and climatology* 50 (2011) 1341–1353.

641 R. Moriwaki, M. Kanda, H. Senoo, A. Hagishima, T. Kinouchi, Anthro-  
642 pogenic water vapor emissions in Tokyo, *Water Resources Research* 44  
643 (2008).

644 Z.-H. Wang, E. Bou-Zeid, J. A. Smith, A spatially-analytical scheme for  
645 surface temperatures and conductive heat fluxes in urban canopy models,  
646 *Boundary-Layer Meteorology* 138 (2011) 171–193.

647 J. Yang, Z.-H. Wang, Land surface energy partitioning revisited: A novel  
648 approach based on single depth soil measurement, *Geophysical Research*  
649 *Letters* 41 (2014) 8348–8358.

650 S. Bateni, D. Entekhabi, Relative efficiency of land surface energy balance  
651 components, *Water Resources Research* 48 (2012).

652 T. Sun, Z.-H. Wang, G.-H. Ni, Revisiting the hysteresis effect in surface  
653 energy budgets, *Geophysical Research Letters* 40 (2013) 1741–1747.

654 J. R. Garratt, The atmospheric boundary layer, *Earth-Science Reviews* 37  
655 (1994) 89–134.

- 656 H. Swaid, Urban climate related aspects of the force-restore method, *Atmo-*  
657 *spheric Environment* 29 (1995) 3401–3409.
- 658 Oke, G. T. Johnson, D. G. Steyn, I. D. Watson, Simulation of surface urban  
659 heat islands under 'ideal' conditions at night part 2: Diagnosis of causation,  
660 *Boundary-Layer Meteorology* 56 (1991) 339–358.
- 661 G. T. Johnson, T. R. Oke, T. J. Lyons, D. G. Steyn, I. D. Watson, J. A.  
662 Voogt, Simulation of surface urban heat islands under 'IDEAL' conditions  
663 at night part 1: Theory and tests against field data, *Boundary-Layer*  
664 *Meteorology* 56 (1991) 275–294.
- 665 S. Miao, W. Jiang, X. Wang, W. Guo, Impact assessment of urban meteorol-  
666 ogy and the atmospheric environment using urban sub-domain planning,  
667 *Boundary-layer meteorology* 118 (2006) 133–150.
- 668 T. Sun, Z. H. Wang, W. C. Oechel, S. Grimmond, The Analytical Objective  
669 Hysteresis Model (AnOHM v1.0): Methodology to determine bulk storage  
670 heat flux coefficients, *Geoscientific Model Development* 10 (2017) 2875–  
671 2890.
- 672 F. Lindberg, K. Olofson, T. Sun, C. Grimmond, C. Feigenwinter, Urban  
673 storage heat flux variability explored using satellite, meteorological and  
674 geodata, *Theoretical and Applied Climatology* (2020) 1–14.
- 675 J. Hrisko, P. Ramamurthy, J. E. Gonzalez, Estimating heat storage in urban

676 areas using multispectral satellite data and machine learning, *Remote*  
677 *Sensing of Environment* 252 (2021) 112125.

678 R. Macdonald, R. Griffiths, D. Hall, An improved method for the estimation  
679 of surface roughness of obstacle arrays, *Atmospheric environment* 32 (1998)  
680 1857–1864.

681 B. Crawford, S. B. Grimmond, A. Gabey, M. Marconcini, H. C. Ward, C. W.  
682 Kent, Variability of urban surface temperatures and implications for aero-  
683 dynamic energy exchange in unstable conditions, *Quarterly Journal of the*  
684 *Royal Meteorological Society* 144 (2018) 1719–1741.

685 J. Wieringa, Roughness-dependent geographical interpolation of surface wind  
686 speed averages, *Quarterly Journal of the Royal Meteorological Society* 112  
687 (1986) 867–889.

688 A. G. Davenport, C. S. B. Grimmond, T. R. Oke, J. Wieringa, Estimating the  
689 roughness of cities and sheltered country, in: *Proceedings 12th Conference*  
690 *on Applied Climatology*, Asheville, NC, American Meteorological Society,  
691 Boston, 2000, pp. 96–99.

692 C. Grimmond, T. R. Oke, Aerodynamic properties of urban areas derived  
693 from analysis of surface form, *Journal of applied meteorology* 38 (1999)  
694 1262–1292.

695 Q. Li, E. Bou-Zeid, S. Grimmond, S. Zilitinkevich, G. Katul, Revisiting  
696 the relation between momentum and scalar roughness lengths of urban

697 surfaces, Quarterly Journal of the Royal Meteorological Society (2020)  
698 1–31.

699 W. Brutsaert, Evaporation into the atmosphere: theory, history and appli-  
700 cations, volume 1, Springer Science & Business Media, 1982.

701 M. Kanda, M. Kanega, T. Kawai, R. Moriwaki, H. Sugawara, Roughness  
702 lengths for momentum and heat derived from outdoor urban scale models,  
703 Journal of Applied Meteorology and Climatology 46 (2007) 1067–1079.  
704 doi:10.1175/JAM2500.1.

705 L. Zhang, J. R. Brook, R. Vet, A revised parameterization for gaseous dry  
706 deposition in air-quality models, Atmospheric Chemistry and Physics 3  
707 (2003) 2067–2082.

708 S. N. Goward, Thermal behavior of urban landscapes and the urban heat  
709 island, Physical Geography 2 (1981) 19–33.

710 J. Wang, R. Bras, G. Sivandran, R. Knox, A simple method for the estimation  
711 of thermal inertia, Geophysical Research Letters 37 (2010).

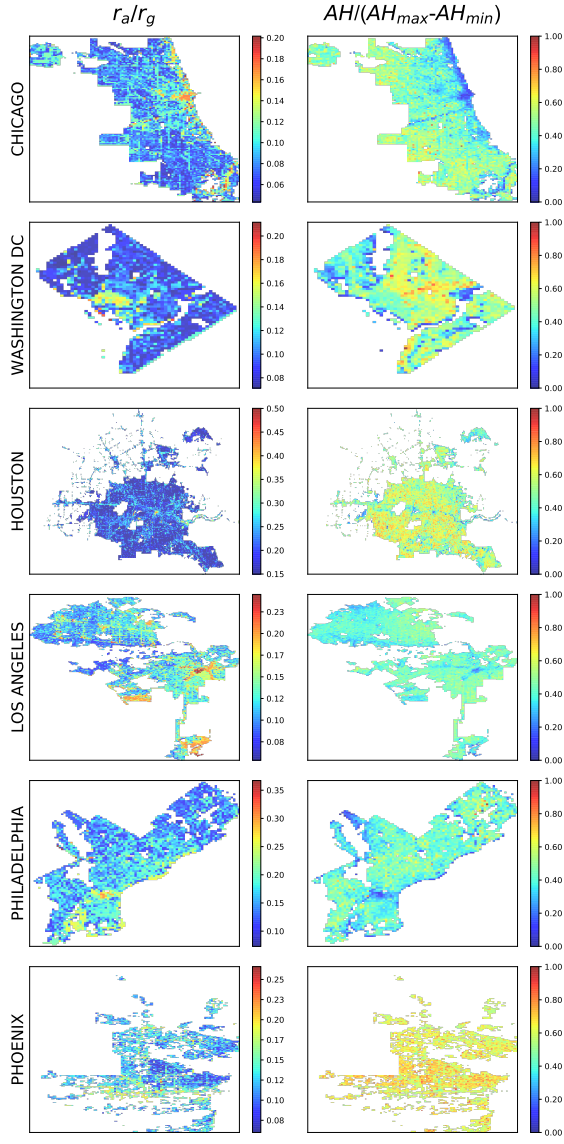


Figure C.5: Six cities: Energy partitioning efficiencies between sensible and storage heat in contrast with scaled AH